Optics Letters

On the transition to secondary Kerr combs in whispering-gallery mode resonators

Aurélien Coillet,[1,2,*] Zhen Qi,[3] Irina V. Balakireva,[1] Guoping Lin,[1,4] Curtis R. Menyuk,[3] and Yanne K. Chembo[1,5,6]

[1]FEMTO-ST Institute, Université Bourgogne Franche-Comté, CNRS, Optics Department, 15B Avenue des Montboucons, 25030 Besançon cedex, France
[2]Laboratoire Interdisciplinaire Carnot de Bourgogne, Université Bourgogne-Franche-Comté, 9 Avenue A. Savary, 21078 Dijon, France
[3]Department of Computer Science and Electrical Engineering, University of Maryland Baltimore County, 1000 Hilltop Circle, Baltimore, Maryland 21250, USA
[4]MOE Key Laboratory of Fundamental Quantities Measurement, School of Physics, Huazhong University of Science and Technology, Wuhan 430074, China
[5]Institute for Research in Electronics and Applied Physics (IREAP), and Department of Electrical and Computer Engineering, University of Maryland, College Park, Maryland 20742, USA
[6]e-mail: ykchembo@umd.edu
*Corresponding author: aurelien.coillet@u-bourgogne.fr

Received 29 March 2019; revised 14 May 2019; accepted 20 May 2019; posted 20 May 2019 (Doc. ID 363770); published 10 June 2019

We demonstrate that extended dissipative structures in Kerr-nonlinear whispering-gallery mode resonators undergo a spatiotemporal instability, as the pumping parameters are varied. We show that the dynamics of the patterns beyond this bifurcation yield specific Kerr comb and sub-comb spectra that can be subjected to a phase of frequency-locking when optimal conditions are met. Our numerical results are found to be in agreement with experimental measurements.

https://doi.org/10.1364/OL.44.003078

Spatiotemporal instabilities arise when a stationary solution loses stability via a traveling wave [1]. Although well-known in the context of the mathematical analysis of nonlinear partial differential equations, unambiguous examples of such instabilities are not very common in nonlinear optics. Noteworthy exceptions include Ref. [2], where the authors analyzed spatiotemporal instability of a constant field (flat state) in a nonlinear medium with both dispersion and diffraction. More recently, Anderson *et al.* investigated theoretically and experimentally the spatiotemporal instability from a temporal cavity soliton in a fiber ring resonator [3].

In this Letter, we analyze the spatiotemporal instabilities of a roll pattern generated in a Kerr-nonlinear whispering-gallery mode resonator. These systems have several important applications in areas such as time-frequency metrology, ultra-stable microwave generation, spectroscopy, and optical telecommunications [4–9]. Despite the fact that Kerr combs have already allowed for many technological applications, the stability of roll patterns is still not fully understood. In particular, emphasis is generally laid on primary bifurcations leading to their emergence, while only a few works have studied the secondary bifurcations leading to their destabilization [10–12]. Indeed, a deep understanding of both primary and secondary bifurcations is key to defining the stability basin for the solutions of technological interest. Here we provide a theoretical explanation for the secondary instabilities of roll patterns and identify them as spatiotemporal instabilities. Our theoretical results are in agreement with the experimental measurements. We also expect this Letter to be of interest for a larger community interested in nonlinear dynamics and pattern formation in spatially extended systems.

The system under investigation is an ultrahigh-Q WGM resonator pumped by a resonant continuous-wave laser [13–16]. The dynamics of the normalized intracavity field $\psi(\theta,\tau)$ obeys the following Lugiato–Lefever equation (LLE) [17–19]:

$$\frac{\partial\psi}{\partial\tau} = -(1+i\alpha)\psi + i|\psi|^2\psi - i\frac{\beta}{2}\frac{\partial^2\psi}{\partial\theta^2} + F, \tag{1}$$

where the normalized parameters are the laser-cavity detuning α, the second-order dispersion β, and the pump field F, while the variables are the dimensionless time τ and the azimuthal angle $\theta \in [-\pi,\pi]$. This equation does not account for the other third-order nonlinearities (Brillouin, Raman, …) of the bulk resonator that could trigger instabilities [20–24].

A wide variety of patterns can be excited inside the resonator [25–30], but the most prevalent extended dissipative structures in the cavity are the so-called Turing roll patterns. These patterns emerge from a flat state via Turing instability and consist of an integer number of rolls along the azimuthal direction of the resonator. Previous theoretical analyses [31,32] have shown that at threshold, this number is the closest integer approximation of $L_{\mathrm{th}} = [2(\alpha-2)/\beta]^{\frac{1}{2}}$.

The Kerr comb spectra corresponding to this roll patterns are sometimes referred to as primary combs, and they feature multiple free spectral range (FSR) spacing, with a multiplicity

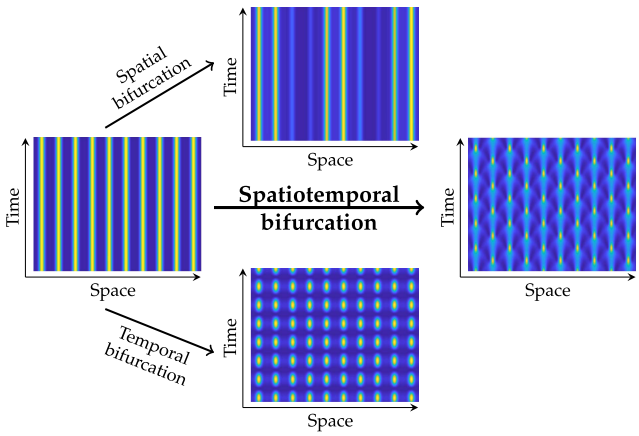

Fig. 1. Illustration of a spatiotemporal bifurcation for the rolls in the LLE. A stable set of Turing rolls, in principle, could undergo several types of bifurcations: a spatial bifurcation will lead to a spatially modulated pattern, while a temporal bifurcation will produce oscillations along the time coordinate. By contrast, a spatiotemporal bifurcation leads to patterns that oscillate in both time and space.

exactly equal to L_{th}. An open question is to understand how these rolls lose their stability, as the pump parameters (power and frequency) are varied. Figure 1 proposes a schematic illustration of the possible destabilization mechanisms for a roll pattern: these mechanisms include temporal, spatial, and spatiotemporal bifurcations. Our main objective in this Letter is to show that it is the latter that governs the destabilization of azimuthal roll patterns in WGM resonators. The stationary solutions of the LLE satisfy Eq. (1) with $\partial_\tau \psi \equiv 0$. Once a steady-state solution ψ_{st} has been found, its stability may be determined by linearizing the LLE about the stationary solution and finding all the eigenvalues of the linearized equation:

$$\frac{\partial}{\partial \tau}\delta\psi = \mathcal{L}\delta\psi, \tag{2}$$

where $\delta\psi = (\delta\psi_{\mathrm{r}}, \delta\psi_{\mathrm{i}})$ is the perturbation with real and imaginary parts $\delta\psi_{\mathrm{r,i}}$, and

$$\mathcal{L} = \begin{pmatrix} -1 - 2\psi_{\mathrm{st,r}}\psi_{\mathrm{st,i}} & \alpha - \psi_{\mathrm{st,r}}^2 - 3\psi_{\mathrm{st,i}}^2 + \frac{\beta}{2}\partial_\theta^2 \\ -\alpha + 3\psi_{\mathrm{st,r}}^2 + \psi_{\mathrm{st,i}}^2 - \frac{\beta}{2}\partial_\theta^2 & -1 + 2\psi_{\mathrm{st,r}}\psi_{\mathrm{st,i}} \end{pmatrix}. \tag{3}$$

The eigenvalue equation $\mathcal{L}\delta\psi = \lambda\delta\psi$ is then used to investigate the stability of the roll patterns. In our computational procedure, we discretize the system by only keeping an even number N of modes in the spectral domain, which can be spanned as

$$\Psi_l = \frac{1}{2\pi}\int_{-\pi}^{\pi} \psi(\theta) e^{-il\theta} \mathrm{d}\theta, \tag{4}$$

with $l = -N/2, \ldots, N/2 - 1$. For the results reported here, we use $N = 512$ or $N = 1024$. We consistently evaluate the second derivative of θ in the wavenumber domain and the nonlinear terms in the θ-domain. Given a good initial guess for a stationary solution, we use the Levenberg–Marquardt algorithm to find the stationary solution. When finding the eigenvalues, the vector $\delta\psi$ of the eigenvalue equation becomes a column vector of length $2N$ after modal expansion. We use a spectral decomposition of the operator ∂_θ^2, which produces dense sub-blocks in the matrix representation of $\mathcal{L}$ [33,34]. We then use the QR algorithm to find all the eigenvalues [35]. We have found that the spectral method adds negligibly to the computer time that we need for our implementations while reducing the angular resolution needed and enabling a direct comparison to our evolutionary studies, based on the split-step Fourier method. We use the boundary-tracking algorithm, described by Wang *et al.* [34], to find the stable operating region for the primary combs. We separately find the stable region for each primary comb of order L, whose comb spacing equals $L \times \mathrm{FSR}$, with L being a positive integer. We fix $\beta = -2.2 \times 10^{-3}$ throughout the Letter, which corresponds to our experiments, and we find the stable regimes in the two-dimensional $\alpha - F^2$ parameter space. To find a stable region for a given value of L, we first find a solution in a highly stable region of the parameter space. We can then determine the stationary solution and its stability as the parameters vary. At some point, the stable solution becomes unstable or ceases to exist. We then move along or track the boundary, as described in Ref. [34]. We note that different bifurcations occur at different points along the boundary, which is why it is important to determine all the eigenvalues. As a consequence, we observe cusps in the boundary of the stable region when shifting from one bifurcation to another. In the laser frequency-power ($\alpha - F^2$) parameter space, Turing rolls with given multiplicity L have defined basins of attraction that can thereby be determined numerically, as shown in Fig. 2.

The spatiotemporal perturbation has a specific signature in both the optical and radio-frequency (RF) domains. Indeed, in the optical domain, the stationary Lth order roll pattern can be expanded as $\psi_{\mathrm{st}}(\theta) = \sum_k \Psi_{kL} e^{ikL\theta}$, with all the Ψ_{kL} being constant. When a spatiotemporal bifurcation occurs, the amplitude of this pattern is perturbed as

$$\psi_{\mathrm{mod}}(\theta, \tau) = [1 + a(\theta, \tau)]\psi_{\mathrm{st}}(\theta), \tag{5}$$

with the traveling-wave perturbation $a(\theta, \tau) = a_0 e^{i(L_a\theta - \Omega_a\tau)}$. In the particular case when $L_a = L/2$, we obtain the so-called secondary combs, and the resulting pattern can be expanded as

$$\psi_{\mathrm{mod}}(\theta, \tau) = \sum_k \Psi_{kL} e^{ikL\theta} + a_0 e^{-i\Omega_a\tau} \sum_k \Psi_{kL} e^{iL\left(k+\frac{1}{2}\right)\theta}, \tag{6}$$

where the first term in the right-hand side stands for the unperturbed pattern ψ_{st}, while the second term stands for the time-dependent, frequency-shifted comb lines created by the

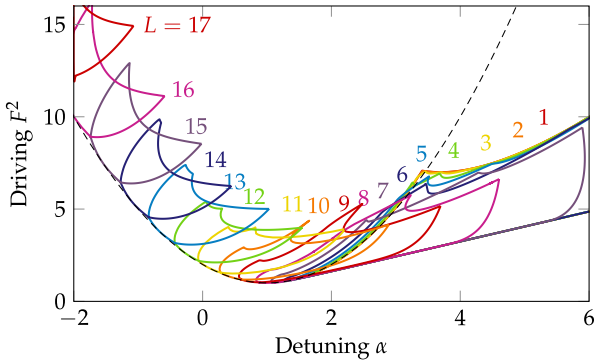

Fig. 2. Stability diagram of the Turing patterns in the parameter space $\alpha - F^2$: within each encompassed area, the Turing pattern with a given number of rolls L is stable.

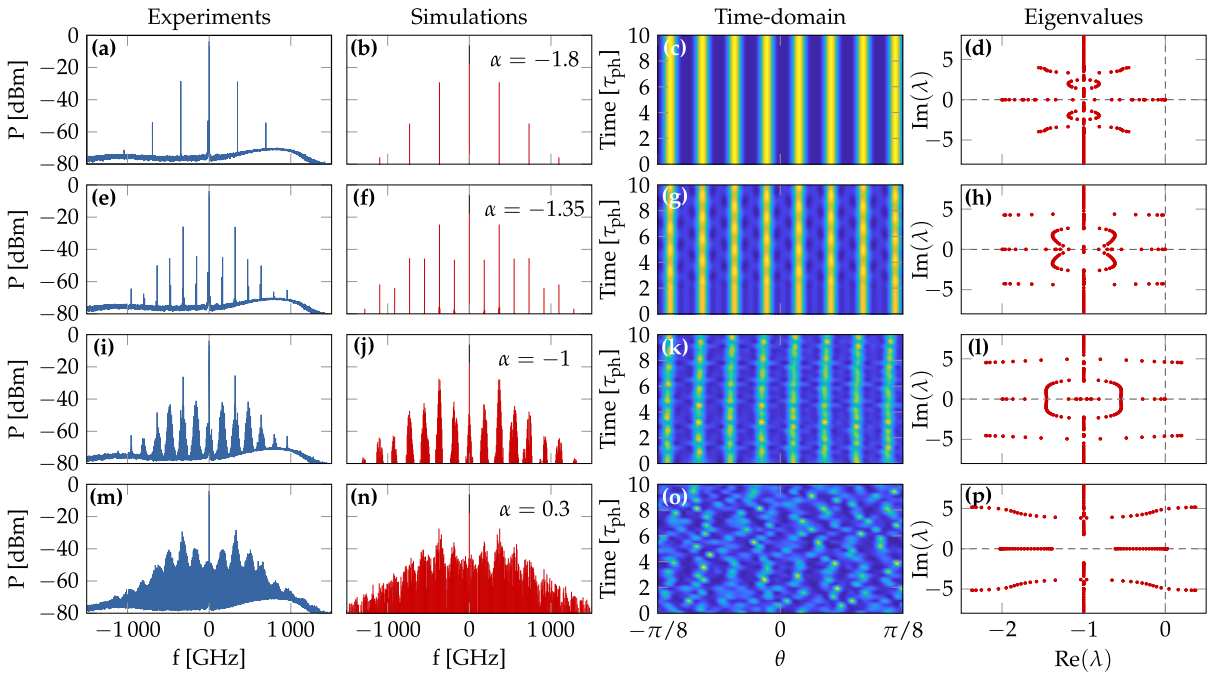

Fig. 3. Experimental transition to secondary combs and chaos obtained with a MgF_2 resonator by detuning the laser further into resonance ($\alpha = -1.8$, -1.35, -1, and 0.3) with constant pump power $F^2 = 12$, corresponding to approximately 100 mW in the experiment. The FSR of the resonator is ~5.9 GHz, and its intrinsic and coupling quality factors are around 10^9 at 1550 nm, corresponding to a photon lifetime $\tau_{ph} = 0.8$ μs. We show corresponding simulation spectra and time-domain evolution in the second and third columns. The last column displays the eigenvalues in the complex plane: the spatiotemporal bifurcation occurs when the real part of one of them becomes positive, close to the detuning $\alpha = -1.35$.

spatiotemporal perturbation. Note that the new spectral components of the secondary comb are located between those of the initial primary comb.

Figure 3 presents a detailed analysis of the spatiotemporal bifurcation, as the laser detuning is varied. The leftmost column corresponds to experimental spectra and shows how, from an initial primary comb with multiplicity $L = 64$, the secondary comb first emerges and then gradually grows towards a fully chaotic comb. The second column displays numerical simulations that are in excellent agreement with the experimental spectra. We note that the LLE matches the experimental data over a large dynamical range (80 dB) and for a high-dimensional system. (There are ~400 oscillating modes in these spectra.) The numerical simulations presented in the third column unveil the dynamics of the rolls as they undergo a spatiotemporal bifurcation. Initially, the roll pattern is stationary with a well-defined stability basin (see Fig. 2), but after the bifurcation, it starts to oscillate both in space and time. This specific dynamics actually corresponds to the modulation of the intensity pattern by a traveling wave following

$$|\psi_{\mathrm{mod}}(\theta,\tau)|^2 \simeq [1 + 2|a_0|\cos(L_a\theta - \Omega_a\tau)]|\psi_{\mathrm{st}}(\theta)|^2, \quad \textbf{(7)}$$

for $|a_0| \ll 1$. Since $L_a \equiv L/2$, the effect of the instability-induced traveling wave a is to trigger antiphase oscillations for adjacent rolls. As the system is driven further from the bifurcation, the pattern enters a regime of spatiotemporal chaos, where the rolls are destroyed. The fourth and last columns of Fig. 3 display the eigenvalue distribution for the cavity modes. It can be seen that the bifurcation occurs when two of these eigenvalues cross the imaginary axis. The crossing of additional pairs of eigenvalue drives the intracavity field into a regime of spatiotemporal optical turbulence.

The spectral signature of the spatial bifurcation can be monitored in the optical spectrum, but the time-averaging of the Fourier spectra does not allow the direct detection of the temporal dynamics for these modes. Instead, the temporal bifurcation can be analyzed via the emergence of modulation side peaks in the photodetected RF spectra of the combs. The comparison between theoretical and experimental results is performed via the output optical signal $\psi_{\mathrm{out}} = -F + 2\rho\psi$, where ρ is the ratio between out-coupling and total losses. After photodetection, an RF signal proportional to the incoming optical power $|\psi_{\mathrm{out}}|^2$ is generated, and features a multi-harmonic signal with spectral components at frequencies $n \times \Omega_{\mathrm{FSR}}$, with $n = 0, 1, 2, \ldots$. The photodetected optical power can be expanded in the Fourier domain as

$$|\psi_{\mathrm{out}}|^2 = \frac{1}{2}\mathcal{M}_0 + \sum_{n=1}^{+\infty}\left[\frac{1}{2}\mathcal{M}_n \exp(in\Omega_{\mathrm{FSR}}t) + \mathrm{c.c.}\right], \quad \textbf{(8)}$$

where $\mathcal{M}_n = 2\sum_l \Psi_{\mathrm{out},l+n}\Psi^*_{\mathrm{out},l}$ is the slowly varying envelope of the microwave spectral component of frequency $n \times \Omega_{\mathrm{FSR}}$, and c.c. stands for the complex conjugate. Therefore, we expect the temporal bifurcation to induce modulation side peaks around $\mathcal{M}_n$, with a spectral spread that is of the order of WGM resonance linewidths (few megahertz). This behavior is experimentally observed in Fig. 4, in agreement with our numerical simulations. These modulation side peaks are due to an interaction with the main modes via four-wave mixing, thereby creating sub-combs that play a major role in

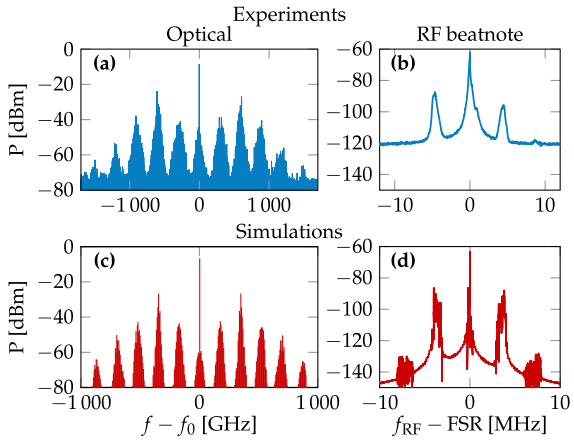

Fig. 4. (a) and (b) Combs and RF beatnotes obtained in a MgF_2 polished resonator in the vicinity of the spatiotemporal instability. (c) and (d) Comb and RF spectra from the numerical simulation of the LLE with $F^2 = 12$ and $\alpha = -1$, demonstrating good agreement with the experimental results.

phase-locking phenomena across the comb [36–39]. Indeed, as the system evolves further from the spatiotemporal bifurcation, the secondary combs in Fig. 3 feature several lines that are created around the initial bifurcation-induced modes. These parasitic lines, spaced by one FSR, are strengthened and amplified by four-wave mixing. They are useful experimentally because without them, we would not be able to photodetect beatnotes around the FSR. The "fundamental" tone would be $(L/2) \times \mathrm{FSR} \sim 150$ GHz away from the FSR, which is beyond the bandwidth of the photodetector.

In conclusion, we have shown that rolls can lose their stability via a spatiotemporal bifurcation that leads to simultaneous oscillations in space and time, corresponding to a traveling-wave amplitude modulation. The resulting pattern can lead to the well-known secondary combs. We expect these results to provide a deeper understanding of the dynamics of many other dissipative structures in WGM resonators [40,41]. In the light of previous research works that already unveiled key mathematical properties of the LLE equation [42–45], we also expect our analysis to lead the way to a stability enhancement of these patterns, for the benefit of the many targeted applications [4–9].

Funding. H2020 European Research Council (ERC) (Versyt PoC 632108, NextPhase StG 278616); Centre National d'Etudes Spatiales (CNES) (SHYRO); National Science Foundation (NSF) (ECCS-1807272).

REFERENCES

1. G. B. Whitham, *Linear and Nonlinear Waves* (Wiley, 1999).
2. L. W. Liou, X. D. Cao, C. J. McKinstrie, and G. P. Agrawal, Phys. Rev. A **46**, 4202 (1992).
3. M. Anderson, F. Leo, S. Coen, M. Erkintalo, and S. G. Murdoch, Optica **3**, 1071 (2016).
4. V. S. Ilchenko and A. B. Matsko, IEEE J. Sel. Top. Quantum Electron. **12**, 15 (2006).
5. T. J. Kippenberg, R. Holzwarth, and S. A. Diddams, Science **332**, 555 (2011).
6. Y. K. Chembo, Nanophotonics **5**, 214 (2016).
7. D. V. Strekalov, C. Marquardt, A. B. Matsko, H. G. Schwefel, and G. Leuchs, J. Opt. **18**, 123002 (2016).
8. G. Lin, A. Coillet, and Y. K. Chembo, Adv. Opt. Photonics **9**, 828 (2017).
9. A. Pasquazi, M. Peccianti, L. Razzari, D. Moss, S. Coen, M. Erkintalo, Y. K. Chembo, T. Hansson, S. Wabnitz, P. Del'Haye, X. Xue, A. M. Weiner, and R. Morandotti, Phys. Rep. **729**, 1 (2018).
10. M. Haelterman, S. Trillo, and S. Wabnitz, Opt. Commun. **93**, 343 (1992).
11. K. Panajotov, M. G. Clerc, and M. Tlidi, Eur. Phys. J. D **71**, 176 (2017).
12. Z. Liu, M. Ouali, S. Coulibaly, M. G. Clerc, M. Taki, and M. Tlidi, Opt. Lett. **42**, 1063 (2017).
13. A. B. Matsko and V. S. Ilchenko, IEEE J. Sel. Top. Quantum Electron. **12**, 3 (2006).
14. A. Chiasera, Y. Dumeige, P. Feron, M. Ferrari, Y. Jestin, G. Nunzi Conti, S. Pelli, S. Soria, and G. C. Righini, Laser Photonics Rev. **4**, 457 (2010).
15. H. Tavernier, P. Salzenstein, K. Volyanskiy, Y. K. Chembo, and L. Larger, IEEE Photonics Technol. Lett. **22**, 1629 (2010).
16. A. Coillet, R. Henriet, K.-P. Huy, M. Jacquot, L. Furfaro, I. Balakireva, L. Larger, and Y. K. Chembo, J. Vis. Exp. **78**, e50423 (2013).
17. A. B. Matsko, A. A. Savchenkov, W. Liang, V. S. Ilchenko, D. Seidel, and L. Maleki, Opt. Lett. **36**, 2845 (2011).
18. Y. K. Chembo and C. R. Menyuk, Phys. Rev. A **87**, 053852 (2013).
19. S. Coen, H. G. Randle, T. Sylvestre, and M. Erkintalo, Opt. Lett. **38**, 37 (2013).
20. H. Rong, S. Xu, Y.-H. Kuo, V. Sih, O. Cohen, O. Raday, and M. Paniccia, Nat. Photonics **1**, 232 (2007).
21. Y. K. Chembo, I. S. Grudinin, and N. Yu, Phys. Rev. A **92**, 043818 (2015).
22. G. Lin and Y. K. Chembo, Opt. Lett. **41**, 3718 (2016).
23. G. Lin, S. Diallo, J. Dudley, and Y. K. Chembo, Opt. Express **24**, 14880 (2016).
24. A. Chen-Jinnai, T. Kato, S. Fujii, T. Nagano, T. Kobatake, and T. Tanabe, Opt. Express **24**, 26322 (2016).
25. P. Del'Haye, A. Schliesser, O. Arcizet, T. Wilken, R. Holzwarth, and T. Kippenberg, Nature **450**, 1214 (2007).
26. Y. K. Chembo and N. Yu, Opt. Lett. **35**, 2696 (2010).
27. T. Herr, V. Brasch, J. Jost, C. Wang, N. Kondratiev, M. Gorodetsky, and T. Kippenberg, Nat. Photonics **8**, 145 (2014).
28. R. Henriet, G. Lin, A. Coillet, M. Jacquot, L. Furfaro, L. Larger, and Y. K. Chembo, Opt. Lett. **40**, 1567 (2015).
29. G. Lin and Y. K. Chembo, Opt. Express **23**, 1594 (2015).
30. L. A. Lugiato, F. Prati, M. L. Gorodetsky, and T. J. Kippenberg, Philos. Trans. R. Soc. London A **376**, 20180113 (2018).
31. C. Godey, I. V. Balakireva, A. Coillet, and Y. K. Chembo, Phys. Rev. A **89**, 063814 (2014).
32. P. Parra-Rivas, D. Gomila, M. A. Matías, S. Coen, and L. Gelens, Phys. Rev. A **89**, 043813 (2014).
33. J. A. C. Weideman and S. C. Reddy, ACM Trans. Math. Software **26**, 465 (2000).
34. S. Wang, A. Docherty, B. S. Marks, and C. R. Menyuk, J. Opt. Soc. Am. B **31**, 2914 (2014).
35. W. H. Press, S. A. Teukolsky, W. T. Vetterling, and B. P. Flannery, *Numerical Recipes* (Cambridge University, 2007).
36. T. Herr, K. Hartinger, J. Riemensberger, C. Y. Wang, E. Gavartin, R. Holzwarth, M. L. Gorodetsky, and T. J. Kippenberg, Nat. Photonics **6**, 480 (2012).
37. J. Li, H. Lee, T. Chen, and K. J. Vahala, Phys. Rev. Lett. **109**, 233901 (2012).
38. P. Del'Haye, K. Beha, S. B. Papp, and S. A. Diddams, Phys. Rev. Lett. **112**, 043905 (2014).
39. K. Saleh and Y. K. Chembo, Opt. Express **24**, 25043 (2016).
40. D. C. Cole, E. S. Lamb, P. Del'Haye, S. A. Diddams, and S. B. Papp, Nat. Photonics **11**, 671 (2017).
41. A. Fulop, M. Mazur, A. Lorences-Riesgo, O. Helgason, P.-H. Wang, Y. Xuan, D. Leaird, M. Qi, P. Andrekson, A. Weiner, and V. Torres-Company, Nat. Commun. **9**, 1598 (2018).
42. T. Miyaji, I. Ohnishi, and Y. Tsutsumi, Physica D **239**, 2066 (2010).
43. G. Kozyreff, Physica D **241**, 939 (2012).
44. C. Godey, Eur. Phys. J. D **71**, 131 (2017).
45. L. Delcey and M. Haragus, Philos. Trans. R. Soc. London A **376**, 20170188 (2018).